Effect of Electronic Coupling on Electron Transfer Rates from Photoexcited Naphthalenediimide Radical Anion to Re(bpy)(CO)₃X

Jose F. Martinez,[†,‖] Nathan T. La Porte,[†,‖] Subhajyoti Chaudhuri,[‡] Alessandro Sinopoli,[§] Youn Jue Bae,[†] Muhammad Sohail,*[,§] Victor S. Batista,*[,†] and Michael R. Wasielewski*[,†]

[†]Department of Chemistry, Center for Light Energy Activated Redox Processes (LEAP), and Institute for Sustainability and Energy at Northwestern, Northwestern University, Evanston, Illinois 60208-3113, United States

[‡]Department of Chemistry, Center for Light Energy Activated Redox Processes (LEAP), and Energy Sciences Institute, Yale University, New Haven, Connecticut 06520, United States

[§]Qatar Environment and Energy Research Institute, Hamad Bin Khalifa University, Education City, P.O. Box, 34110, Doha, State of Qatar

Ⓢ Supporting Information

ABSTRACT: The electron transfer rate between a donor and an acceptor depends on the free energy change for the reaction as well as differences in structure and electronic coupling between the initial and final states. Selective excitation of a naphthalenediimide radical anion (NDI•⁻) covalently linked at the 4-, 5-, or 6-positions of the bipyridine (bpy) in the Re(bpy)(CO)₃X (X = Cl or pyridine) carbon dioxide reduction catalyst results in electron transfer from ²*NDI•⁻ to Re(bpy)(CO)₃X to form Re(bpy•⁻)(CO)₃X, the first intermediate in the photocatalytic reduction of CO₂. Femtosecond UV/vis, near-IR, and mid-IR spectroscopy on these constitutional isomers and a set of appropriate reference molecules show that systematically varying the electronic coupling as well as the reaction free energy increases the lifetime of Re(bpy•⁻)(CO)₃X by an order of magnitude when the NDI chromophore is attached to the 6-position of bpy. NMR and X-ray structural studies along with computational modeling are used to identify the conformation of Re(6-NDI-bpy)(CO)₃X responsible for these favorable changes. Extending the lifetime of the reduced complex in the covalent photosensitizer−catalyst assembly is a critical requirement for the photocatalytic CO₂ reduction and artificial photosynthesis.
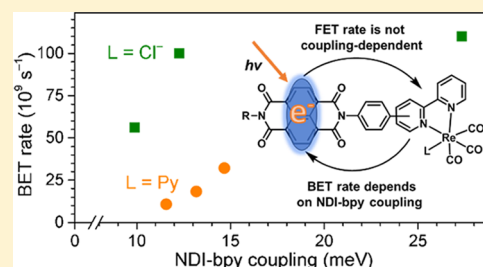
INTRODUCTION

As rising concentrations of CO₂ in the atmosphere continue to impact global climate change, artificial photosynthesis offers an approach to mitigate its effects by using solar energy to transform CO₂ into fuel in a manner analogous to natural photosynthesis.[1] A key challenge of artificial photosynthesis is developing an understanding of how photoinduced electron transfer (ET) reactions can lead to long-lived charge separation (CS), which in turn provides the redox equivalents necessary to carry out bond-forming reactions.[2,3] The molecular architectures present in photosynthetic reaction center proteins provide bioinspiration for developing molecular assemblies that can perform rapid photodriven CS to produce radical ion pairs that undergo slow charge recombination (CR). For example, chlorophyll molecules in the photosystem II reaction center protein complex of green plants absorb solar photons, resulting in the oxidation of the P680 special pair chlorophyll dimer which in turn oxidizes an adjacent tyrosine. This tyrosine functions as a redox intermediate that transfers oxidizing equivalents from P680•⁺ to the water splitting CaMn₄ cluster. In conjunction with this process, electrons are relayed to the photosystem I protein complex to reduce oxidized

nicotinamide adenine dinucleotide phosphate, which plays a vital role in converting CO₂ into glucose.[1,4]

The photocatalytic utility of rhenium polypyridyl complexes for CO₂ photoreduction was first studied in the 1980s by Lehn, Ziessel, and Hawecker, who demonstrated that the complex could reduce CO₂ to CO with high efficiency and selectivity.[5] One of the best-characterized transition metal complexes for homogenous catalytic CO₂ reduction is *fac*-Re(bpy)(CO)₃X (bpy = 2,2′-bipyridine), where X is a wide variety of monodentate coordinating ligands.[6−8] Researchers inspired by the high efficiency and selectivity of these catalysts have explored different avenues to improve the observed catalytic rate and stability. To improve photo- and electrocatalytic performance, researchers have tuned the steric hindrance and redox potentials of the complex by substituting the bpy ring with a variety of different functional groups, most commonly at the 4-position,[8−10] less commonly at the 5-position,[11,12] and rarely at the 6-position. Modification of the X ligand has also been pursued; for example, Kubiak has demonstrated that

placing different substituents (R = OCH$_3$, CH$_3$, tBu, H, CN, CF$_3$) on the bpy of the archetypal Re(4,4′-R-bpy)(CO)$_3$X complexes alters the first reduction potential of the complex, whereas changing the X ligand (X = Cl, Br, Py(OTf), or CH$_3$CN(OTf), OTF = trifluoromethanesulfonate) affects both the first and second redox potentials.[8] Ultimately, the electron-donating ability of the 4,4′-substituent determines the first redox potential and stability of the corresponding electro-catalyst,[8] whereas complexes having the same 4,4′-substituents but different X ligands have similar electrocatalytic CO$_2$ reduction activity. In turn, Ishitani has shown that photo-catalytic CO$_2$ reduction by Re(bpy)(CO)$_3$X, where X is a series of different coordinating phosphine ligands, makes the first reduction of Re(bpy)(CO)$_3$X more negative and improves its photocatalytic CO$_2$ reduction activity.[7]

Covalently linking photosensitizers to the Re-based CO$_2$ reduction catalysts using the 4,4′-positions of bpy is by far the most common approach to these functional dyads. Ishitani developed supramolecular Re(bpy)(CO)$_3$X systems by co-valently attaching Ru-based chromophores to Re(bpy)-based catalysts at the 4-position of bpy to form Ru^{II}(dmb)$_3$-Re^I(dmb)(CO)$_2$L$_1$L$_2$.[7] The Perutz group developed metal-loporphyrins that link through the 4-position of bpy to form [Re^I(CO)$_3$(3-picoline)-4-bpy-MTPP][OTf], where M = Zn or Mg, OTF = trifluoromethanesulfonate, and TPP = tetraphe-nylporphyrin.[13] Recently, quarterpyridine (qpy), which can be viewed as two bipyridines linked to one another via the 5-position of bpy, was utilized as a binding ligand to form the [(bpy)$_2$Ru^{II}]-[qpy]-[Re(CO)$_3$Cl] dinuclear complexes.[12] Elec-tron transfer to Re(bpy)(CO)$_3$X via the 6-position of bpy is rare, and no direct electron transfer through a bridge covalently attached to that site has been demonstrated. However, Gray and Grubbs demonstrated that linking phenothiazine (PTZ) via a tris(*m*-phenyleneethynylene) bridge to form Re(PTZ-tris(*m*-phenyleneethynylene)-6-bpy)(CO)$_3$Py results in a 20 Å through-space distance between the PTZ and Re(bpy)-(CO)$_3$Py. This complex is capable of folding in on itself to form a structural conformer that brings the PTZ donor within 7 Å of the Re(bpy)(CO)$_3$Py, which upon photoexcitation of the complex undergoes through-space electron transfer from PTZ to the complex.[14] The energetics of charge-separated species are directly related to the charge separation lifetimes and are intrinsically related to photocatalytic CO$_2$ reduction efficiency.[15,16] These processes demonstrate the importance of balancing structure, energetics, and electronic coupling between electron donors and acceptors, which is embodied in Marcus electron transfer theory, as given by eq 1

$$k_{ET} = \frac{2\pi |H_{DA}|^2}{\hbar \sqrt{4\pi\lambda k_B T}} \exp\left(-\frac{(\Delta G° + \lambda)^2}{4\lambda k_B T}\right) \quad (1)$$

where $\Delta G°$ is the standard free energy change for the ET reaction, λ is the structure-dependent nuclear reorganization energy, H_{DA} is the electronic coupling between the donor and acceptor, T is the temperature, and k_B is Boltzmann's constant.

In light of these examples of electron transfer to Re(bpy)-(CO)$_3$X through the 4-, 5-, and 6-positions of bpy in Re(bpy)(CO)$_3$X complexes, we decided to systematically investigate the electron transfer rates from a photosensitizer to Re(bpy)(CO)$_3$X. We recently demonstrated the utility of naphthalene-1,4:5,8-bis(dicarboximide) (NDI) and perylene-3,4:9,10-bis(dicarboximide) (PDI) radical anions as chromo-phores bound through the 4-position of bpy in [Re(bpy)-

(CO)$_3$Py][PF$_6$] complexes.[17] The lowest excited doublet states of NDI$^{•-}$ and PDI$^{•-}$ are all-organic super-reductants that can be readily prepared by mild reduction with tetrakis(dimethylamino)ethylene (TDAE)[17−19] or via a platinum electrode followed by photoexcitation with visible or near-infrared light to yield ^{2*}NDI$^{•-}$ and ^{2*}PDI$^{•-}$ having excited-state oxidation potentials of −2.1 and −1.75 V vs saturated calomel electrode (SCE), respectively, which exceed those of most metalorganic/organometallic chromophores. Not only do these radical anion chromophores absorb light throughout the entire visible and NIR region, they can be covalently linked to many organic and organometallic electron acceptors using well-developed synthetic techniques, and their very negative excited-state oxidation potentials allow them to reduce thermodynamically demanding substrates like Re(bpy)-(CO)$_3$X and successive intermediates in its catalytic cycle.

Our previous work demonstrated that attaching NDI to the 4-position of bpy with a phenyl spacer to form [Re(4-bpy-NDI)(CO)$_3$Py][PF$_6$] (see Figure 1) and photoexciting
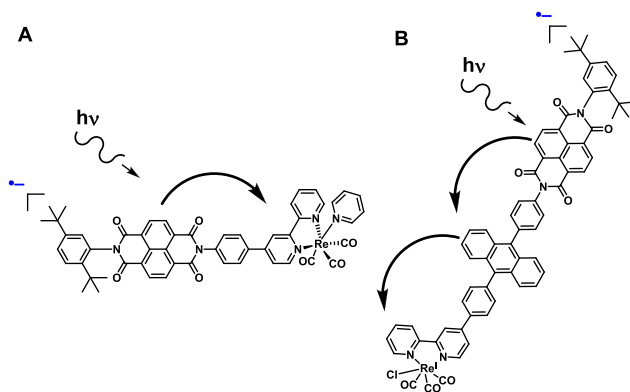
Figure 1. Photoinduced electron transfer from NDI$^{•-}$ to Re(bpy)-(CO)$_3$ via NDI−Ph− (A) and NDI−DPA− (B).

chemically generated NDI$^{•-}$ results in a forward electron transfer (FET) reaction from ^{2*}NDI$^{•-}$ to [Re(bpy)(CO)$_3$Py]-[PF$_6$] in τ_{FET} = 0.4 ± 0.3 ps to form [Re(bpy$^{•-}$)(CO)$_3$Py]-[PF$_6$] followed by back electron transfer (BET) to the ground state in τ_{BET} = 31.8 ± 0.8 ps. By including a 9,10-diphenylanthracene (DPA) intermediate acceptor between the ^{2*}NDI$^{•-}$ and Re(bpy)(CO)$_3$X, transient absorption experiments show that the photoexcitation of NDI$^{•-}$ and subsequent two-step electron transfer produces Re(4-bpy$^{•-}$-DPA-NDI)(CO)$_3$Cl, which has a lifetime of τ_{BET} = 24.5 ± 0.2 ns, nearly 3 orders of magnitude longer than the dyad.

In the present report, we describe the synthesis, electro-chemistry, time-resolved UV/vis/NIR/mid-IR spectroscopy, and calculated electronic couplings for the electron transfer reactions in molecular dyads comprising NDI$^{•-}$ covalently linked through a phenyl bridge to the 4-, 5-, and 6-positions of bpy to give Re(bpy-Ph-NDI)(CO)$_3$X complexes (Scheme 1). Covalently attaching the NDI$^{•-}$ photosensitizer to different positions on the bpy modifies the electronic coupling between the photosensitizer and the catalyst, whereas changing the X ligand alters the free energy of reaction for the reduction of the Re complex, which affects both the photo- and electrocatalytic properties of Re(bpy)(CO)$_3$X complexes.

Chemical reduction of Re(bpy-NDI)(CO)$_3$X with tetrakis-(dimethylamino)ethylene (TDAE) is used to selectively reduce NDI to NDI$^{•-}$[17−19] to form Re(bpy-NDI$^{•-}$)(CO)$_3$X

Scheme 1. Synthetic Scheme for Re(4-,5-,6-bpy-NDI)(CO)$_3$Cl (1, 2, 3) and [Re(4-,5-,6-bpy-NDI)(CO)$_3$Py][PF$_6$] (4, 5, 6)
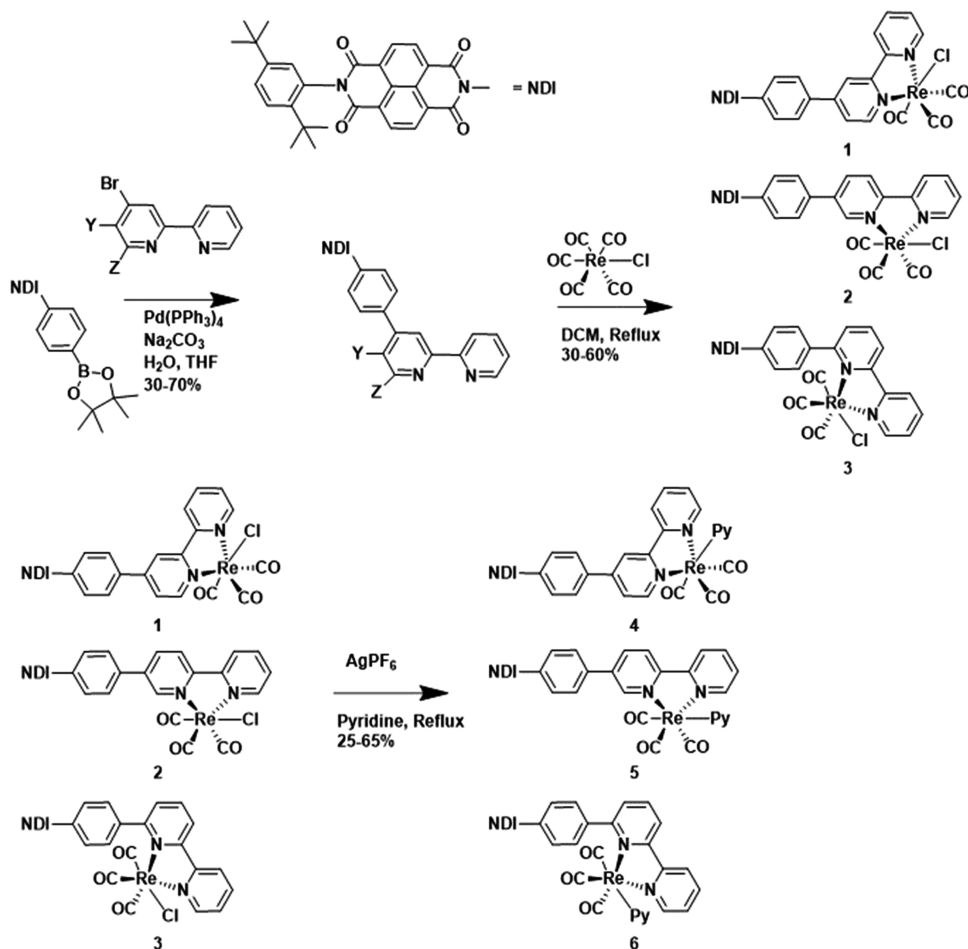
($1^{\bullet-}$–$6^{\bullet-}$) (See Scheme 1 for structures corresponding to each compound number). Selective excitation of NDI$^{\bullet-}$ at 605 nm first yields the excited-state ^{2*}NDI$^{\bullet-}$, which undergoes oxidative quenching to transfer an electron to Re(bpy)(CO)$_3$X, leading to the formation of Re(bpy$^{\bullet-}$)(CO)$_3$X. Transient absorption spectroscopy on complexes $1^{\bullet-}$–$6^{\bullet-}$ yields similar spectral features but different kinetics. FET occurs in $\tau_{FET} \cong 1$ ps, whereas BET occurs in $\tau_{BET} \cong 10–100$ ps, with the trend τ_{BET} (3) > τ_{BET} (2) > τ_{BET} (1) and τ_{BET} (6) > τ_{BET} (5) > τ_{BET} (4). Comparing the charge transfer time constants in chloro- and pyridine-ligated complexes demonstrates that when the location of the NDI$^{\bullet-}$–Ph fragment is kept constant, ΔG_{BET} primarily determines τ_{BET}, resulting in pyridine-substituted complexes with longer τ_{BET} than their neutral counterparts: τ_{BET} (6) > τ_{BET} (3), τ_{BET} (5) > τ_{BET} (2), and τ_{BET} (4) > τ_{BET} (1). In contrast, by changing the substituent location of NDI$^{\bullet-}$–Ph around bpy but keeping same X ligand, ΔG_{BET} does not determine the τ_{BET} values, but instead the electronic coupling $|H_{DA}|$ dominates.

The electronic coupling, $|H_{DA}|$, was computed for the BET reaction [Re(bpy)(CO)$_3$X$^{\bullet-}$][NDI] → [Re(bpy)(CO)$_3$X]-[NDI$^{\bullet-}$], for each complex, which illustrates that $|H_{DA}|$ decreases as the NDI–Ph moves among the 4-, 5-, and 6-positions of bpy with the trend H_{DA}^B (1) > H_{DA}^B (2) > H_{DA}^B (3) and H_{DA}^B (4) > H_{DA}^B (5) > H_{DA}^B (6). These results correlate with the observed trends in the lifetimes of the respective charge-shifted species, whereas ΔG_{BET} does not. Thus, the electronic coupling $|H_{DA}^B|$ between the NDI$^{\bullet-}$–Ph substituent

and Re(bpy)(CO)$_3$Cl at the 4-, 5-, and 6-positions of bpy is the key factor governing the electron transfer rate.

■ EXPERIMENTAL SECTION

Materials. Dichloromethane, acetone, acetonitrile, and methanol used for synthesis were obtained from Fisher Scientific and used as received. Dimethylformamide (DMF) used for synthesis and spectroscopic experiments was dried on a commercial system (Pure Process Technology). For spectroscopy, DMF was further transferred under argon into a N$_2$-filled glovebox (MBraun Unilab) for use and storage. Commercially available reagents were purchased from Sigma-Aldrich or Oakwood Chemicals and used as received. Compounds were reduced in the glovebox using tetrakisdiaminoethylene (TDAE) from Tokyo Chemical Industries. Detailed synthetic procedures and compound characterization are shown in the Supporting Information (SI). UV/vis/NIR absorption spectroscopy was performed on a Shimadzu UV-1601 spectrometer at 298 K.

Electrochemistry. Electrochemical measurements were performed using a CH Instruments Model 660A electrochemical workstation. A single-compartment cell was used for all cyclic voltammetry experiments with a 1.0 mm diameter glassy carbon disk working electrode, a platinum wire counter electrode, a silver wire pseudoreference electrode, and 0.1 M tetrabutylammonium hexafluorophosphate as the supporting electrolyte in DMF. The ferrocene/ferrocenium redox couple (0.45 V vs SCE)[20] was used as an internal standard. TBAPF$_6$

Scheme 2. Synthetic Scheme for Re(4-,5-,6-Ph-bpy)(CO)$_3$Cl (7−9)
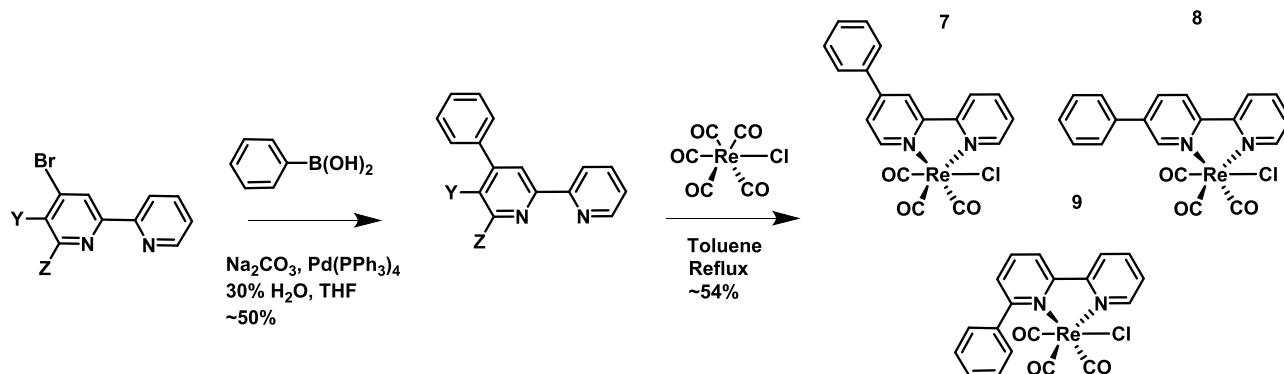
was recrystallized twice from ethanol prior to use. Electrochemical cells were shielded from light during experiments. All solutions were purged with argon before and after each cyclic voltammetry experiment. Solutions of rhenium complexes were prepared in a concentration of 0.5 mM for cyclic voltammetry experiments.

Femtosecond Transient Vis/NIR Absorption Spectroscopy. Femtosecond transient absorption experiments employed a regeneratively amplified Ti:sapphire laser system operating at 828 nm with a 1 kHz repetition rate, as previously described.[21,22] The output of the amplifier was frequency-doubled to 414 nm using a BBO crystal, and the 414 nm light was used to pump a laboratory-built collinear optical parametric (OPA) amplifier for visible-light excitation[23] or a commercial noncollinear optical parametric amplifier (TOPAS-White, Light-Conversion, LLC) for NIR excitation. Approximately 1−3 mW of the fundamental was focused onto a CaF$_2$ disk to generate the visible white-light probe spanning 330−800 nm or onto a proprietary medium (Ultrafast Systems, LLC) to generate the NIR white-light probe spanning 850−1620 nm. The total instrument response function was 300 fs. Experiments were performed with a depolarized pump to suppress contributions from orientational dynamics. Spectral and kinetic data were collected with a complementary metal-oxide-semiconductor or InGaAs array detector for visible and NIR detection, respectively, and an 8 ns pump-probe delay track (customized Helios, Ultrafast Systems, LLC). Transient spectra were averaged for at least 3 s. Gaps in the spectra shown are due to either scattering of the pump or idler beam or regions not covered by the detectors. Samples prepared in DMF had an absorbance of 0.2−0.7 at the excitation wavelength and were irradiated in 2 mm quartz cuvettes with 0.4−0.8 μJ/pulse focused to an ∼0.2 mm diameter spot. Samples were stirred to avoid effects of local heating or sample degradation. The samples were prepared in the glovebox.

Nanosecond Transient Absorption Spectroscopy. Nanosecond transient absorption experiments were performed using the femtosecond excitation beam described above and a commercial spectrometer (Eos, Ultrafast Systems, LLC) utilizing a photonic crystal fiber ultrabroadband probe source. The pump polarization was randomized to suppress rotational dynamics. Samples were stirred to avoid the effects of local heating or sample degradation.

Femtosecond Time-Resolved Mid-IR (fsIR) Spectroscopy. Femtosecond transient mid-IR absorption (fsIR) spectroscopy was performed using a commercial Ti:sapphire oscillator/amplifier (Solstice 3.5 W, Spectra-Physics) to pump

two optical parametric amplifiers (TOPAS-C, Light Conversion), one of which provided a 100 fs, 605 nm excitation pulse and the other 100 fs pulses at 2150−1800 cm^{-1}. The overall instrument response time was 500 fs. The spectra were acquired with a liquid N$_2$-cooled dual channel (2 × 64) MCT array detector that is coupled to a Horiba HR320 monochromator as part of a Helios-IR spectrometer (Ultrafast Systems, LLC). Samples with a maximum optical density of 1.5 at the excitation wavelength were prepared in DMF contained in a liquid demountable cell (Harrick Scientific) with 2.0 mm thick CaF$_2$ windows and a 500 μm Teflon spacer. During data acquisition, the cell was mounted and rastered on a motorized stage to prevent sample degradation.

Computational Methods. Density functional theory (DFT) calculations were performed using a combination of the Gaussian 09[24] and QChem 5.0[25] software packages. Geometry optimizations were performed at B3LYP/6-31G+(d)[26] level of theory in the presence of polarizable continuum DMF solvent implemented using the C-PCM solvation model[27] in Gaussian 09. A double zeta effective core potential basis (LANL2DZ)[28] was used for the Re atom in all of the above-mentioned calculations. To reduce computational cost, the *t*-butyl groups were replaced by methyl groups, since the *t*-butyl substituent does not affect the spectroscopic properties of such complexes. To consider thermal fluctuations, multiple configurations were obtained by performing constrained optimizations keeping a dihedral, φ, between the NDI and Re(bpy)(CO)$_3$X$^{\bullet-}$ parts of the complexes fixed at different values in increments of 30°. The constrained optimizations were done in Gaussian 09 at B3LYP/Def2SVP[24] level of theory in a SMD[29] dielectric continuum of DMF. Electronic couplings $|H_{DA}(\varphi)|$ were computed using the direct diabatic-state method[30] implemented in QChem 5.0[25] at HF/Def2TZVP level of theory. A C-PCM[31] dielectric continuum solvent model of DMF was used in all of the coupling calculations.

■ **RESULTS**

Synthesis. Complexes **1** (Re(4-bpy-NDI)(CO)$_3$Cl), **2** (Re(5-bpy-NDI)(CO)$_3$Cl), **3** (Re(6-bpy-NDI)(CO)$_3$Cl), **4** ([Re(4-bpy-NDI)(CO)$_3$Py][PF$_6$]), **5** ([Re(5-bpy-NDI)-(CO)$_3$Py][PF$_6$]), and **6** ([Re(6-bpy-NDI)(CO)$_3$Py][PF$_6$]) were prepared as illustrated in Scheme 1 and detailed in the SI. NDI−Ph−Bpin[32] was Suzuki coupled[33] to the corresponding 4-, 5-, or 6-bromo-2,2′-bipyridine to form the corresponding 4-, 5-, or 6-phenyl-NDI-2,2′-bipyridine. Each ligand was then refluxed in dry dichloromethane under nitrogen with pentacarbonylchlororhenium(I) to form **1−3**. Complexes **1−3**
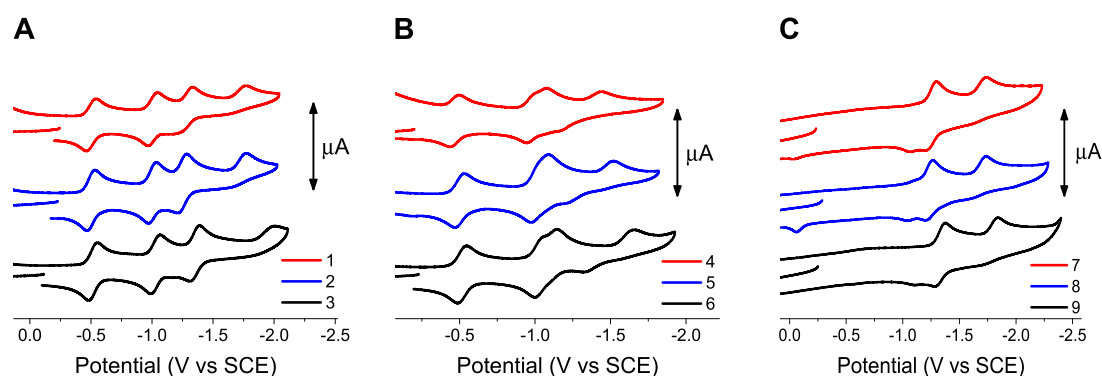
Figure 2. Cyclic voltammograms of 0.5 mM DMF solutions of complexes **1−3** (A), **4−6** (B), and **7−9** (C), recorded at 100 mV s^{-1} at room temperature with 0.1 M TBAPF$_6$ as a supporting electrolyte. Potentials are reported versus SCE (Fc/Fc$^+$ occurs at 0.45 V vs SCE in DMF).

were then heated to 80 °C in pyridine with silver hexafluorophosphate to yield their respective pyridine complexes, **4−6**.

Model complexes **7−9** were synthesized, as illustrated in Scheme 2 and detailed in SI. The corresponding 4-, 5-, or 6-bromo-2,2′-bipyridine was Suzuki coupled to phenylboronic acid. Each ligand was then refluxed in dry dichloromethane under nitrogen with pentacarbonylchlororhenium(I) to form **7−9**. Complex **10** is unsubstituted Re(bpy)(CO)$_3$Cl.

Electrochemistry. Cyclic voltammetry experiments were performed on **1−6** to measure the effect of including an NDI−phenyl substituent on the redox potentials as well as to estimate the free energy change for photoinduced electron transfer from ^{2*}NDI$^{•-}$ to the corresponding bound rhenium complex shown in Figure 2. Cyclic voltammetry experiments were conducted on **7−9** to explore the influence the phenyl substituent alone has on the redox properties of each rhenium complex. Cyclic voltammetry redox potentials for each complex are shown in Figure 2, and their redox potentials are tabulated in Table 1.

Table 1. Redox Potentials of 1−10 vs SCE (Fc/Fc$^+$ Reference at 0.45 V vs SCE in DMF)

complex	NDI$^{0/-}$	NDI$^{-/2-}$	bpy$^{0/-}$	Re−L$^{I/0}$
1	−0.51	−1.02	−1.34	−1.77
2	−0.50	−1.01	−1.29	−1.77
3	−0.52	−1.01	−1.39	−2.01
4	−0.49	−1.00	−1.08	−1.47
5	−0.50	−1.01	−1.10	−1.52
6	−0.52	−1.03	−1.15	−1.67
7			−1.31	−1.75
8			−1.27	−1.74
9			−1.40	−1.86
10			−1.35	−1.80

For complexes **1−3**, where the rhenium complex has a bound chloride ligand, the cyclic voltammogram first displays two reductions near −0.51 and −1.01 V vs SCE, respectively. These reversible processes are the formation of NDI$^{•-}$ and (NDI^{2-}). These reductions are followed by the one-electron reduction of the bpy ligand to bpy$^{•-}$ between −1.25 and −1.36 V. A subsequent irreversible one-electron reduction of the rhenium center (Re−Cl$^{I/0}$) follows, coinciding with the loss of the chloride ligand. For **1** and **2**, the reduction of the rhenium center occurs at −1.77 V, whereas in **3**, this reduction occurs at −2.01 V, a 240 mV difference.

For **4−6**, where the rhenium complex has a bound pyridine ligand and is positively charged, the voltammogram first displays two reductions near −0.50 and −1.01 V. These reversible reduction processes again correspond to the formation of NDI$^{•-}$ and NDI^{2-}. These reductions are followed by the one-electron reduction of the bpy ligand between −1.08 and −1.15 V. A subsequent one-electron irreversible reduction of the rhenium center follows. For **4** and **5**, this reduction occurs at −1.45 and −1.52 V, respectively, whereas in **6**, this reduction occurs at −1.67 V.

Complexes **7−9** display two reduction peaks; the first reduction corresponds to the reduction of the coordinated bpy, and the second reduction corresponds to the reduction of the rhenium center, which coincides with the loss of the chloride ligand. During the reverse scan, a small anodic peak appears for each complex that is slightly more positive than the bpy$^{0/-}$ anodic wave. This anodic wave represents the reoxidation of the reduced complexes [Re(R-bpy$^{•-}$)(CO)$_3$(DMF)] formed following the dissociation of Cl$^-$ from the respective radical anion complexes and rapid coordination of the solvent ligand.[6]

Electron Transfer Energetics. Based on the redox potentials shown above, the free energy changes for the excited-state electron transfer reactions of **1$^{•-}$−6$^{•-}$** can be estimated using the following equation

$$\Delta G_{ET} = E(NDI^{•-}/NDI) - E(A^{•-}/A) - E_{D_I}(^{2*}NDI^{•-})$$

(2)

where $E(NDI^{•-}/NDI)$ is the reduction potential of NDI, $E(A^{•-}/A)$ is the reduction potential of the complex of interest, and E_{D_I} is the energy of the ^{2*}NDI$^{•-}$ excited doublet state, assuming that electron transfer occurs from the D$_1$ state. The D$_1 \leftarrow$ D$_0$ transition of NDI$^{•-}$ absorbs at 785 nm, making $E_{D_1} =$ 1.58 eV. There is no electrostatic work term for this reaction because the reaction is a charge shift from anionic NDI$^{•-}$ and neutral bpy to neutral NDI and anionic bpy$^{•-}$, not a charge separation. Therefore, there is no additional Coulombic attraction or repulsion in the charge-shifted state relative to the ground state. In addition, there is no solvation correction term because the fsTA and electrochemical experiments are performed in the same high polarity solvent. Therefore, the free energy change for the thermal forward and back electron transfer reactions can be estimated using the following equation

$$\Delta G_{ET} = E(A^{•-}/A) - E(NDI^{•-}/NDI)$$

(3)

Using the equations above, the free energy changes for each electron transfer step were calculated and are given in Table 2.

Table 2. Free Energy Changes for Electron Transfer Reactions in complex $1^{\bullet-}-6^{\bullet-}$

compound	process	ΔG (eV)
$1^{\bullet-}$	$*NDI^{\bullet-} \rightarrow Re(4\text{-bpy})Cl$	−0.75
$2^{\bullet-}$	$*NDI^{\bullet-} \rightarrow Re(5\text{-bpy})Cl$	−0.79
$3^{\bullet-}$	$*NDI^{\bullet-} \rightarrow Re(6\text{-bpy})Cl$	−0.71
$4^{\bullet-}$	$*NDI^{\bullet-} \rightarrow Re(4\text{-bpy})Py$	−0.99
$5^{\bullet-}$	$*NDI^{\bullet-} \rightarrow Re(5\text{-bpy})Py$	−0.98
$6^{\bullet-}$	$*NDI^{\bullet-} \rightarrow Re(6\text{-bpy})Py$	−0.95
$1^{\bullet-}$	$Re(4\text{-bpy}^{\bullet-})Cl \rightarrow NDI^0$	−0.83
$2^{\bullet-}$	$Re(5\text{-bpy}^{\bullet-})Cl \rightarrow NDI^0$	−0.79
$3^{\bullet-}$	$Re(6\text{-bpy}^{\bullet-})Cl \rightarrow NDI^0$	−0.87
$4^{\bullet-}$	$Re(4\text{-bpy}^{\bullet-})Py \rightarrow NDI^0$	−0.59
$5^{\bullet-}$	$Re(5\text{-bpy}^{\bullet-})Py \rightarrow NDI^0$	−0.60
$6^{\bullet-}$	$Re(6\text{-bpy}^{\bullet-})Py \rightarrow NDI^0$	−0.63

Steady-State Spectroscopy. Complexes **1−6** all exhibit similar steady-state spectroscopic features in both the UV/vis/NIR and mid-IR regions. Representative steady-state spectra for **6** are shown in Figure 3, and the full set of spectra is given in the Supporting Information (Figures S1, S3, S5, S7, S9, and S11).

Before reduction by TDAE, the electronic absorption spectra exhibit the strong narrow absorbance bands characteristic of neutral NDI at 381 and 361 nm.[18] Underneath these absorbances and tailing into the visible region is the broad metal to ligand charge transfer (MLCT) absorbance of the $Re(bpy)(CO)_3L$ fragment, which peaks between 340 and 360 nm depending on the complex. In general, Cl-substituted **1−3** have MLCT bands whose maxima are redder than the Py-substituted **4−6**.[34] In addition to this variation, **2** and **5**, which feature substitution at the 5-bpy position, have MLCT bands that tail further into the visible region, giving solutions of these complexes a distinctive orange color compared to solutions of the other complexes. Upon reduction, the neutral NDI peaks disappear and are replaced by peaks at 471, 605, 700, and 795 nm characteristic of the $NDI^{\bullet-}$,[18] whereas the MLCT absorbance remains unchanged.

In the mid-IR, three peaks are observed in the carbonyl stretching region; with the two lower-energy peaks sometimes overlapping to form one broad peak. The high-energy peak (around 2000−2050 cm^{-1}) corresponds to the high-energy in-phase symmetric vibration of the three CO ligands, and the lower-energy peaks (around 1850−1950 cm^{-1}) correspond to the out-of-phase symmetric vibration of the three CO ligands and the antisymmetric vibration of the two equatorial CO ligands.[35] The splitting of the two low-energy peaks in **6**, uncommon in Py-ligated complexes, of this type, is indicative of an asymmetric environment for the CO ligands in this complex, as will be discussed below. Py-ligated complexes have stretches that are shifted to higher energy relative to the analogous complexes with Cl$^-$ ligands, reflective of the lower electron density on the Re center and weakening the Re−C backbonding and strengthening the C≡O bond. As expected, reduction of the NDI fragment does not affect these vibrational peaks.

Time-Resolved Vis/NIR/Mid-IR spectroscopy. The FET and BET kinetics upon excitation of the $NDI^{\bullet-}$ in $1^{\bullet-}-6^{\bullet-}$ were probed using a combination of femtosecond time-resolved visible/NIR (fsTA) and time-resolved mid-IR (fsIR) spectroscopy. The oxidation state of the NDI moiety was monitored in the visible/NIR region, whereas the oxidation state of the $Re(bpy)(CO)_3X$ fragment was monitored in the mid-IR. A representative set of fsTA and fsIR spectra, acquired on $6^{\bullet-}$, are shown in Figures 4 and 5 together with the kinetic analysis of the data. Data for all six complexes can be found in the Supporting Information (Figures S1−S12).

Singular value decomposition (SVD) was used to analyze the fsTA data, as described in our previous papers.[17] SVD produces a set of kinetic and spectral basis vectors which are fit to a specified kinetic model using a least-squares fitting algorithm to determine the lifetimes for each kinetic component. These kinetic components are then used to calculate species-associated spectra for each decay lifetime. For all six compounds $1^{\bullet-}-6^{\bullet-}$, the fsTA data were fit to an A → B → G(round state) model, where A is assigned to $^2*NDI^{\bullet-}$ and B is assigned to the charge-shifted state $NDI^0-Re(bpy^{\bullet-})-(CO)_3X$. The FET and BET rate constants determined from analysis of the fsTA data are presented in Table 3. The quantum yield of FET was estimated by comparing the intrinsic $^2*NDI^{\bullet-}$ excited-state lifetime ($\tau = 141$ ps) with its lifetime in each complex.[18] Because the IR spectrum is insensitive to the oxidation or excitation state of the NDI moiety, the fsIR data were analyzed using a multiple-wavelength global fitting procedure that fit the kinetics of the B → G process only. Although it is theoretically possible to determine the A → B kinetics by fitting the rise time of the signals corresponding to state B, that the rise time is extremely
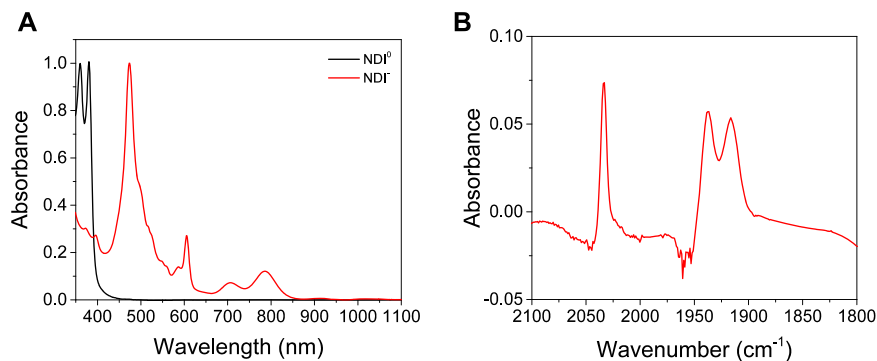
Figure 3. UV/vis/NIR (A) and mid-IR (B) steady-state spectra of **6** in DMF without (black) and with excess TDAE (red). The mid-IR spectrum is identical in the presence or absence of TDAE.
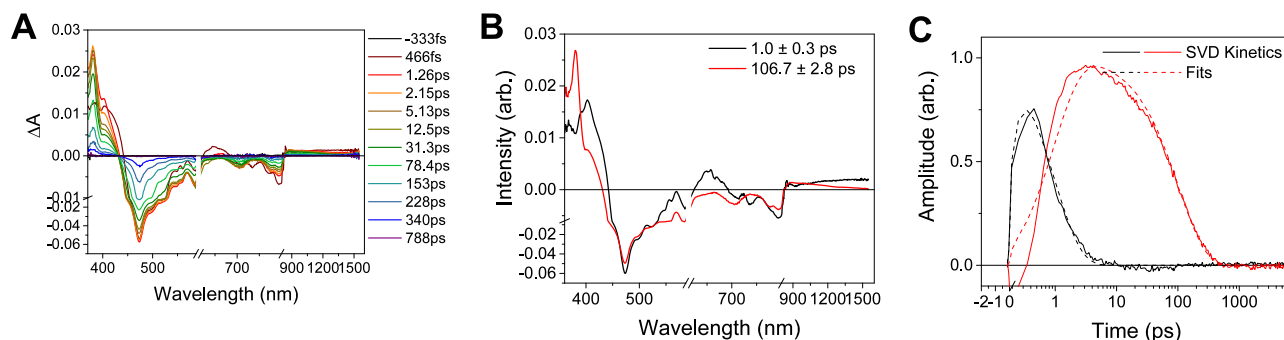
Figure 4. (A) fsTA spectrum of **6** in DMF with excess TDAE (λ_{ex} = 605 nm). (B) Species-associated spectra obtained from global analysis of TA data using singular value decomposition (SVD) kinetic traces. Best-fit lifetimes of each spectral component are given in the legend. (C) Kinetic traces (solid) and fits (dashed) obtained by SVD of fsTA data. Best-fit lifetimes are given in the legend for the species-associated spectra.
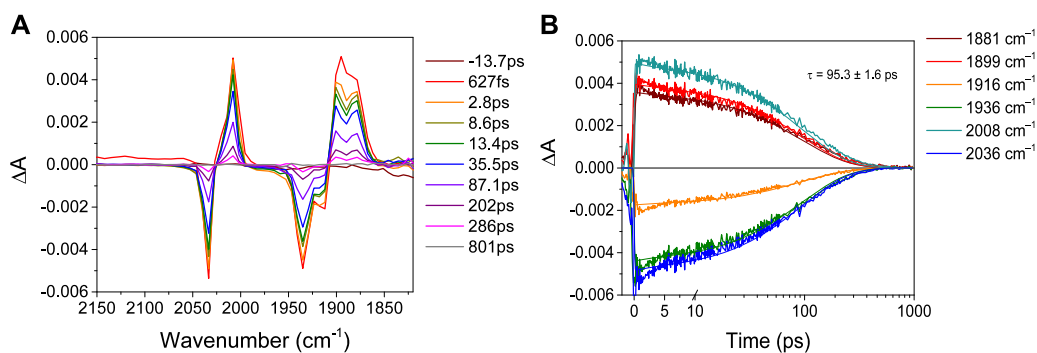

Figure 5. Left: fsIR spectrum of **6** in DMF with excess TDAE (λ_{ex} = 605 nm). Right: Kinetic traces and fits to the lifetime shown of the fsIR at the given frequencies.

Table 3. FET and BET Kinetic Data for $1^{\bullet-}$−$6^{\bullet-}$ in DMF with Excess TDAE (λ_{ex} = 605 nm) Obtained by an Analysis of fsTA Spectra

complex	X	τ_{FET} (ps)	k_{FET} (s^{-1})	τ_{BET} (ps)	k_{BET} (s^{-1})	Φ_{FET}
$1^{\bullet-}$	Cl$^-$	1.2 ± 0.3	8.3 × 10^{11}	9.5 ± 0.7	1.1 × 10^{11}	0.99
$2^{\bullet-}$	Cl$^-$	1.1 ± 0.3	9.1 × 10^{11}	10.0 ± 0.4	1.0 × 10^{11}	0.99
$3^{\bullet-}$	Cl$^-$	1.3 ± 0.3	7.7 × 10^{11}	17.8 ± 0.3	5.6 × 10^{10}	0.99
$4^{\bullet-}$	Py	0.4 ± 0.3	2.5 × 10^{12}	32 ± 1	3.1 × 10^{10}	0.99
$5^{\bullet-}$	Py	1.5 ± 0.3	6.7 × 10^{11}	59 ± 4	1.7 × 10^{10}	0.99
$6^{\bullet-}$	Py	1.0 ± 0.3	1.0 × 10^{12}	107 ± 2	9.4 × 10^{9}	0.99
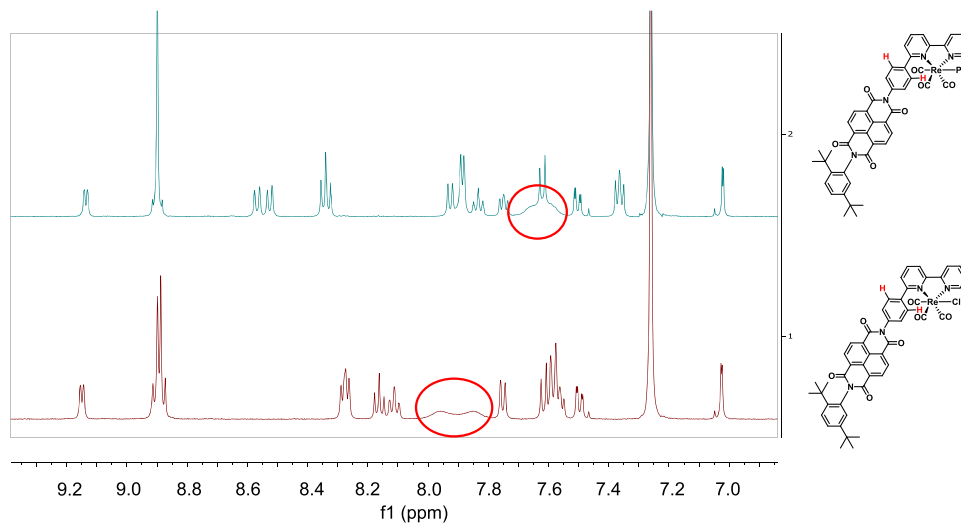
Figure 6. ^{1}H NMR of complexes **6** (top) and **3** (bottom). Broadening of two protons on their respective phenyl substituent is circled.
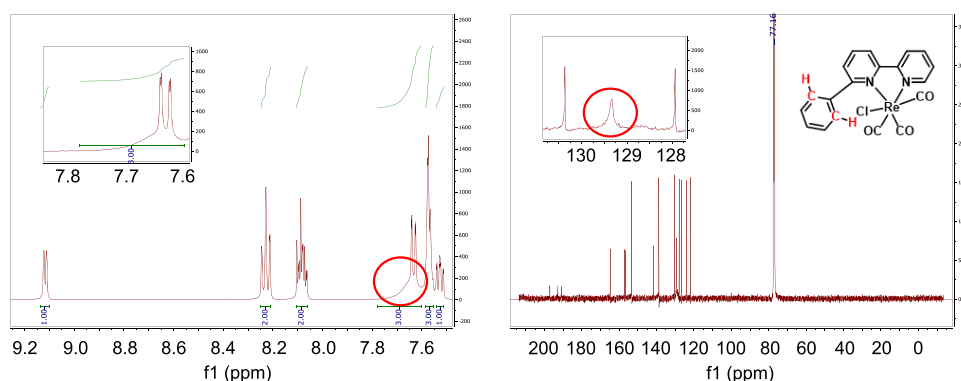
Figure 7. ^{1}H NMR (left) and ^{13}C NMR (right) of complex **9**. Broadening of two protons and carbons on the phenyl substituent is illustrated.

short (<2 ps, see below), and fsIR signals that appear within 1−2 ps of $t = 0$ are occluded by a strong coherence artifact and so cannot be fit accurately (Figure 5).

Structural Studies. The ^{1}H NMR spectra of **3** and **6** show a significant broadening of the resonances assigned to the two protons on the phenyl ring (Figure 6). No broadening of the ^{1}H NMR resonances occurs in the 4- or 5-substituted Re(bpy-NDI)(CO)$_3$X complexes. Additionally, there is no broadening of protons in the bare ligands of any bpy ligand investigated in this study. To obtain better insight into the broadening of the ^{1}H NMR resonances, the model complex Re(6-Ph-bpy)-(CO)$_3$Cl (**9**) was investigated further. The ^{1}H NMR spectrum of **9** shows a significant broadening of two phenyl protons (Figure 7), whereas the rest of the phenyl and bpy protons appear sharp, as is the case for Re(6-bpy-NDI)(CO)$_3$Cl and Re(6-bpy-NDI)(CO)$_3$Py. The ^{13}C NMR spectrum of **9** shows a significant broadening of the carbon atoms attached to these protons, whereas the remaining bpy and phenyl carbons are single sharp peaks. ^{1}H and ^{13}C NMR assignments were further confirmed via correlation spectroscopy (COSY), heteronuclear single quantum correlation (HSQC), and carbon distortionless enhancement by polarization transfer (DEPT) experiments (Figures S14−S19). The broadening in the ^{1}H and ^{13}C NMR spectra of **9** is associated with restricted rotation of the protons and carbons because of the proximity of the phenyl to the metal center.

To verify this interaction, crystals of **9** suitable for X-ray diffraction were grown by vapor diffusion of diethyl ether into a solution of **9** dissolved in dichloromethane. The diffraction data reveal a molecular structure similar to those reported previously for Re compounds[11] with a pseudo-octahedral arrangement of ligands around a rhenium center (Figure 8), consistent with IR data that demonstrate that the carbonyl ligands adopt facial geometries (see also SI Tables S1 and S2). The carbons at the 8- and 9-positions of **9** are closest to the nearest carbonyl, as indicated by the crystal structure; this interaction likely broadens the proton and carbon resonances. Previous work done using 6-phenyl-2,2′-bipyridine (HL) as a coordinating ligand (N,N donor) to form Ru(HL)$_2$Cl$_2$ showed a significant broadening of the phenyl substituent protons in the ^{1}H NMR spectrum, whereas the bpy protons appeared sharp.[36] Additionally, the HL ligand could be utilized as a C, N, N-donor in metal complexes that incorporated Rh. The phenyl substituent was found to form an organometallic (carbon-metal) bond and formed the cyclometallated complex Rh-HL(MeCN)Cl$_2$, illustrating the HL's close proximity to the metal center.[36]
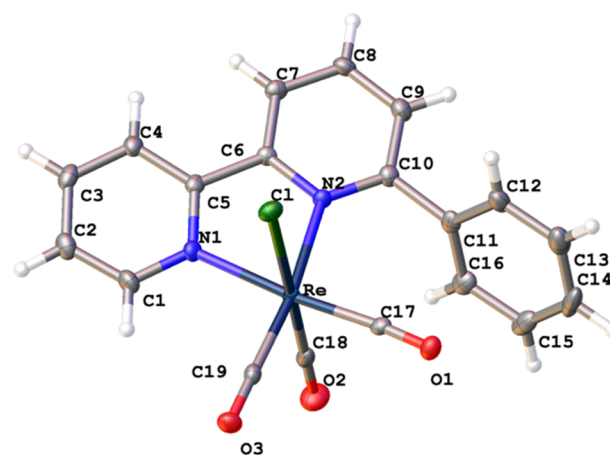
Figure 8. X-ray crystallographically derived the molecular structure of complex **9**.

The through-space interaction between the phenyl and the metal complex also likely increases the dihedral angle between the bpy ligand and the phenyl ring, as observed in the DFT-optimized geometries. In the 6-bpy complexes, the dihedral angle $\varphi \approx 54°$, in comparison to the 4- and 5-bpy complexes where $\varphi \approx 38°$. This increased dihedral angle decreases the coupling between the phenyl ring and the bpy ligand in the 6-bpy substituted complexes relative to the 4- and 5-bpy substituted complexes, in which no phenyl−Re interaction occurs.

Computed Molecular Orbitals (MOs) and Geometries. In the absence of crystal structures for most of the reported complexes, the optimization of the ground-state geometry for the reported complexes revealed structural information fundamental for understanding some of the experimental properties. As reported in Table 4, the distance between the rhenium and both equatorial carbonyl ligands is approximately 1.93 Å for all of the complexes except for those with a substituent in position 6 relative to the bpy. In this case (**3**, **6**, and **9**), the Re−CO distance for the carbonyl pointing away from the substituted position 6 was about 0.02 Å shorter than for the opposite equatorial carbonyl. On the other side, both axial ligands were unaffected by the different bipyridyl ligands. We attribute the asymmetry between the two equatorial carbonyls to the strong distortion of the two pyridyl rings in the 6-substituted bpy ligands. This asymmetry gives rise to a splitting of the low-energy peaks in the vibrational spectrum of this complex, as discussed above. The 4- and 5-substituted bpy show a quasi-coplanarity of the two rings, whereas the 6-

Table 4. Computed Geometry Parameters for the Investigated Complexes

compound #	$d_{Re-COeq}$/Å	$d_{Re-COax}$/Å	d_{Re-X}/Å	Θ_{py-py}/deg	Θ_{py-ph}/deg
1	1.930;1.929	1.920	2.513	0.033	−40.681
2	1.929;1.930	1.919	2.512	0.109	39.698
3	1.917;1.942	1.914	2.520	9.919	54.788
4	1.934;1.934	1.937	2.275	−0.803	−35.19
5	1.934;1.934	1.937	2.274	0.652	36.25
6	1.921;1.947	1.930	2.276	10.667	53.22
7	1.930;1.929	1.919	2.513	−0.393	−39.260
8	1.929;1.929	1919	2.512	0.290	38.267
9	1.916;1.940	1.914	2.517	10.054	54.612

substituted bpy ligands present a dihedral angle of 10°. For the 6-substituted bipyridyl ligands, the dihedral angle between the substituted ring and the phenyl fragment results in more distortion than for the 4- and 5-substituted bpy ligands, at $\varphi \approx 54°$ instead of $\varphi \approx 38°$.

The frontier orbital distributions of **1**, **4**, and **7** are depicted in Figure 9. The localization of specific orbitals was found to be
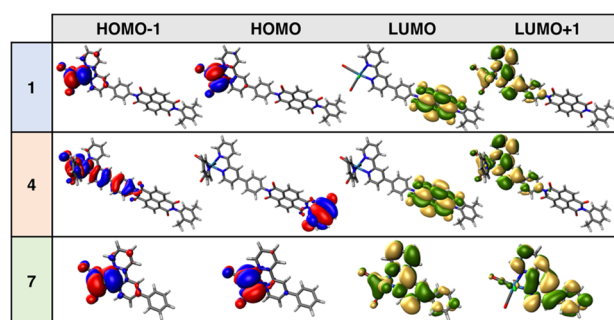

Figure 9. Optimized geometries and plots of HOMO − 1, HOMO, LUMO, and LUMO + 1 orbitals for complexes **1**, **4**, and **7**.

unchanged within each of the three sets of complexes; the remaining complexes are shown in the SI. For all of the neutral investigated complexes, the highest occupied molecular orbital (HOMO) and HOMO − 1 are predictably localized between the rhenium, the halogen, and the three carbonyl ligands with minimal (HOMO − 1) or no contribution (HOMO) arising from the ancillary ligand. For the cationic analogs, the energies of occupied MOs become stabilized enough to alter the distribution pattern seen in Figure 10 (**1** and **7**). Therefore, the HOMO for the pyridine-substituted complexes is located on the NDI substituent, whereas the bpy pyridyl rings contribute together with the metal and the carbonyls to the HOMO − 1. In the NDI complexes **1−6**, the lowest unoccupied molecular
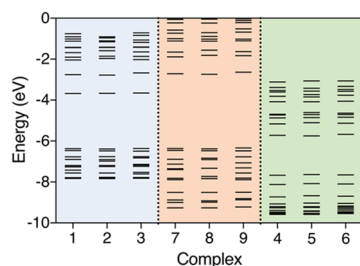

Figure 10. Calculated molecular orbital energy level diagram for complexes **1−9**. Model complexes **7−9** are displayed next to **1−3** to better appreciate the effect of the NDI fragment.

orbital (LUMO) is dominated by the NDI fragment, whereas the LUMO + 1 is bpy-centered. Model complexes **7−9** have both LUMO and LUMO + 1 localized on the bpy−Ph ligand.

Kohn−Sham energy diagrams for the 10 highest occupied and 10 lowest unoccupied MOs for **1−9** are shown in Figure 10, and Frontier orbital energies are summarized in Table 5.

Table 5. Calculated HOMO and LUMO Energies for Complexes 1−9

compound	HOMO (eV)	LUMO (eV)	$\Delta_{HOMO-LUMO}$ (eV)	$\Delta_{HOMO-LUMO}$ (nm)
1	−6.373	−3.676	2.696	460
2	−6.385	−3.668	2.717	456
3	−6.359	−3.658	2.700	459
4	−7.674	−5.723	1.952	635
5	−7.640	−5.746	1.894	654
6	−7.654	−5.670	1.984	625
7	−6.362	−2.716	3.646	340
8	−6.378	−2.740	3.638	341
9	−6.339	−2.639	3.700	335

With orbitals mainly delocalized on the Re(CO)$_3$Cl core, the HOMO energies for the neutral complexes **1−3** and **7−9** lie at about −6.3 eV. Complexes **1−3** display almost identical LUMO energies, likely a result of the NDI-centered charge localization. Similarly, LUMO + 1 for complexes **1−3** and LUMO for **7−9** have similar energies due to the similar orbital distribution across the common Re(bpy)(CO)$_3$Cl fragment. The energies for the cationic species shift to lower energies relative to the corresponding neutral complexes, this is attributed to the effect of the positive charge of these systems. Comparing the HOMO−LUMO gap of the neutral and the cationic complexes shows that the replacement of a π-donor (the halogen) with a π-accepting ligand (pyridine) induces a destabilization of the HOMO, hence a narrower HOMO−LUMO gap.

Thermally Averaged Electronic Coupling. Electronic coupling depends strongly on the relative orientation of the donor and acceptor, which can vary due to thermal fluctuations. Electronic couplings $|H_{DA}(\varphi)|$ were computed for the BET reaction [Re(bpy)(CO)$_3$X$^{\bullet-}$][NDI] → [Re-(bpy)(CO)$_3$X][NDI$^{\bullet-}$]. The thermally averaged couplings were obtained by taking the energetically feasible conformations of the complexes at room temperature (selected using a cutoff of 1 kcal/mol on the energies of the complexes, Figure 11A,B) and Boltzmann averaging the electronic couplings $|H_{DA}(\varphi)|$ computed for those conformations were done using eq 4.[37]
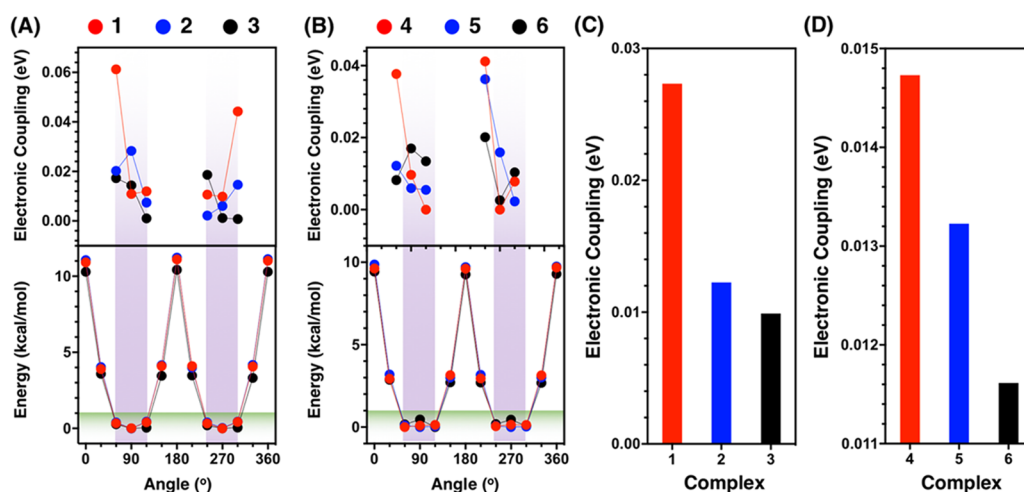
Figure 11. (A) (Bottom) Energies for different structures of complexes **1**, **2**, and **3** obtained by scanning the dihedral between Re(bpy)(CO)$_3$Cl$^{\bullet-}$ and NDI and (top) electronic couplings for the BET for structures with energies < 1 kcal/mol. (B) (Bottom) Energies for different structures of complexes **1**, **2**, and **3** obtained by scanning the dihedral between Re(bpy)(CO)$_3$Py$^{\bullet-}$ and NDI and (top) electronic couplings for the back-ET for structures with energies <1 kcal/mol. Boltzmann averaged electronic couplings |H_{if}^B| for back-ET complexes (C) **1**, **2**, and **3** and (D) **4**, **5**, and **6**.

$$H_{DA}^B = \frac{\sum_i |H_{DA}(\varphi)| e^{-\Delta E_i(\varphi)/kT}}{\sum_i e^{-\Delta E_i(\varphi)/kT}} \qquad (4)$$

■ DISCUSSION

The electrochemical data shown in Table 1 reveal that the attachment of the NDI−Ph to Re(bpy)(CO)$_3$X has a negligible effect on the reduction potentials of NDI. The first two reductions for **1**−**6** are NDI localized and are similar to those of the free NDI chromophore.[18] Despite that having NDI−Ph substituted onto the bpy slightly perturbs the two reduction potentials of Re(bpy)(CO)$_3$X. For example, in complexes **1**−**3**, the bpy reductions are separated by 100 mV, whereas their Re−Cl$^{I/0}$ pairs are separated by 240 mV. To explain this disparity, we synthesized model rhenium complexes that do not have an NDI chromophore attached at the 4-, 5-, or 6-bpy position to isolate the effects that the Ph− and NDI−Ph have on the reduction potentials of Re(bpy)(CO)$_3$Cl. In comparison to **7**, the reduction potentials (bpy$^{0/-}$ and Re−Cl$^{I/0}$) of the unsubstituted Re(bpy)(CO)$_3$Cl (**10**) shift to more positive potentials. This is attributed to the extended conjugation from the bpy into the phenyl substituent, lowering the bpy π^* orbital energy and making the bpy$^{0/-}$ reduction more facile. This is likely the same reason for the anodic shift observed in **8** compared to **10**. This is unsurprising given the greater electronic coupling and conjugation from bpy onto the phenyl, shifting the redox potentials more positive. In contrast, for **9**, where the bpy is substituted at the 6-position with a phenyl, the bpy$^{0/-}$ and Re−Cl$^{I/0}$ reductions instead shift to more negative potentials. The X-ray crystal structure of **9** shows the proximity of the phenyl substituent to the metal center. It can be seen from the calculated electronic structure that the LUMO of the phenyl−bpy ligands extends onto the appended phenyl ring, despite the increased twist of the phenyl ring relative to the bpy ligand as discussed above. Therefore, as the complex gets reduced, some negative charge comes to reside on that phenyl ring. Because the Re center is positively charged, it is likely that as the complex gets reduced, the complex electrostatically repels this phenyl substituent, making the reduction of **9** more difficult. This does not occur

in **7** and **8**, due to the different geometry which maintains the distance between the phenyl ring and the Re center. This conclusion is additionally supported by ^{1}H NMR and ^{13}C NMR, as the phenyl group on **9** has broadened the ^{1}H NMR and ^{13}C NMR lines, indicating a lack of free rotation, caused by the close proximity of the phenyl to metal complex, whereas **7** and **8** do not. This rationale can be extended to **1**−**6**, where in the case of **3** and **6**, the metal complex must repel the phenyl that has a bulky NDI substituent linked to it. This leads to more negative reduction potentials for the metal complex than their constitutional isomer counterparts, see Table 1. Similar results have been observed by Ishitani, who constructed Ru− Re complexes that were separated by an alkyl bridge.[7,38] When the length of the alkyl bridge was decreased from 6 to 4 to 2 carbons, they observed a through-space interaction that changed the Re(dmb)(CO)$_3$Cl reduction potential.

When comparing the reduction potentials of **1**−**3** to **4**−**6**, the third reduction (bpy$^{0/-}$) occurs at more negative potentials; this reflects the destabilization of the bpy π^* orbital by the Cl$^-$ ligand due to the chloride's ability to be a π-donor in contrast to the pyridine ligand.[6] This effect, in addition to **4**−**6** being positively charged, has a more drastic effect on the fourth reduction (Re−X$^{I/0}$) where the metal-based reductions shift by ∼230 mV to the positive with a pyridine bound than in **1**−**3** with a chloride bound. With respect to ΔG_{BET} for **1**$^{\bullet-}$− **6**$^{\bullet-}$, only the reduction potentials of bpy are of concern, as we are interested in the reduction of Re(bpy-NDI$^{\bullet-}$)(CO)$_3$X to Re(bpy$^{\bullet-}$-NDI^0)(CO)$_3$X. The electrochemical data in Table 1 illustrate that by substituting the chloride ligand for pyridine, ΔG_{BET} for Re(bpy$^{\bullet-}$)(CO)$_3$X → NDI^0 is decreased by 200− 300 mV for **1**−**3** relative to their pyridine counterparts. This will have implications for the BET rate that will be discussed later.

Whether the NDI$^{\bullet-}$−Ph substituent is at the 4-, 5-, or 6- positions of bpy on Re(bpy)(CO)$_3$X, the same photophysical processes occur upon selective excitation of NDI$^{\bullet-}$ at λ_{ex} = 605 nm, albeit with different kinetics. At short times, the fsTA spectra show instrument-limited bleaches of the ground-state NDI$^{\bullet-}$ features at 471, 700, and 795 nm, induced absorptions attributable to ^{2*}NDI$^{\bullet-}$ at 403 nm, and in the region 600− 1500 nm, which overlap the bleaches at 700 and 795 nm. As

the fsTA spectra evolve, the bleaches remain, but the $^2*NDI^{•-}$ induced absorptions decay. In their place, an induced absorption at 381 nm appears, characteristic of NDI^0 (in some datasets an additional induced absorption at 361 nm is also visible, although this wavelength lies just at the edge of detectability in the fsTA apparatus and is not always observable). In the NIR, a broad induced absorption attributable to the $Re(bpy^{•-})(CO)_3L$ moiety is observed to grow in with the same kinetics as the growth of the NDI^0 band(s). The strength and wavelength of that band vary with the site of substitution on the bpy and with the nature of X, although it always corresponds to the SOMO → LUMO + n transition, the orbitals of which are located on the bpy ligand. Because the bpy ligand is partially conjugated to the Ph substituent, shifting the location of substitution affects the relative energies of the bpy-centered orbitals and consequently the spectra of the reduced $Re(bpy)(CO)_3L$ fragment.

The fsIR spectra are quite similar to those obtained from our previous experiments for similar rhenium complexes.[17,32,39] Upon reduction, the ground-state absorptions bleach, and induced absorptions appear at lower energies. A shift to lower energy of the CO stretching frequencies is commonly observed when the bpy ligand on the Re is reduced, due to the increased electron density on the Re center strengthening the π-backbonding to the CO and weakening the CO bond.[10] These induced absorptions are observed to decay with kinetics identical within experimental error to the kinetics of the B → G process observed in the fsTA data. Due to a large coherence artifact that obscures the first ~2 ps of fsIR data, as discussed above, kinetic fittings of these data, especially for complexes with shorter BET lifetimes, are less accurate than lifetimes obtained from fitting the fsTA data.

For all of the complexes studied, τ_{FET} is <2 ps. This reflects the fact that in all of the complexes, ΔG_{FET} is large enough that electron transfer occurs within or near the barrierless region of the Marcus curve and is not observably affected by the differences in ΔG_{FET}. However, when comparing τ_{BET} for complexes with the $NDI^{•-}$−Ph chromophore at same substituent position of bpy but with different X ligands (e.g., $1^{•-}$ vs $4^{•-}$), we see that the BET rate decreases. For example, τ_{BET} = 9.5 ± 0.7 ps for $1^{•-}$, in contrast to τ_{BET} = 32 ± 1 ps for $4^{•-}$. It is clear that by substituting Cl^- for pyridine, ΔG_{BET} becomes less negative as well, leading to a slower BET lifetime. This trend is consistent when comparing all of the τ_{BET} values between $1^{•-}$ and $3^{•-}$ and their counterparts $4^{•-}$ and $6^{•-}$. In comparing τ_{BET} for complexes with the $NDI^{•-}$−Ph chromophore at a different substituent location on bpy but with the same X ligand (e.g., $1^{•-}$ vs $2^{•-}$ vs $3^{•-}$), we see that the τ_{BET} is slower. In the set of complexes with a Cl^- ligand, the complex with $NDI^{•-}$−Ph at the 6-position has a more negative ΔG_{BET} than the complexes with $NDI^{•-}$−Ph at the 4- or 5-positions but a slower BET time constant (τ_{BET} = 17.8 ± 0.3 for $3^{•-}$ vs τ_{BET} = 9.5 ± 0.7 ps for complex $1^{•-}$). In the set of complexes with a pyridine bound ($4^{•-}$−$6^{•-}$), the values of ΔG_{BET} are quite similar. Despite that fact, the values of τ_{BET} among the three complexes are quite different, with τ_{BET} being ~3 times longer in $6^{•-}$ than in $4^{•-}$. It is clear that the location of the $NDI^{•-}$−Ph substituent on bpy plays a role in determining τ_{BET}, but the slower BET times cannot be rationalized using ΔG_{BET}. As seen in Figure 11C,D, $|H^B_{DA}|$ for BET in Re(4-,5-,6-bpy-NDI)(CO)$_3$Cl shows the trend H^B_{DA} (**1**) > H^B_{DA} (**2**) > H^B_{DA} (**3**) resulting in the observed BET trend of τ_{BET} (**1**) < τ_{BET} (**2**) < τ_{BET} (**3**). Likewise in [Re(4-,5-,6-bpy-NDI)(CO)$_3$Py][PF$_6$],

the computed trend of H^B_{DA} (**4**) > H^B_{DA} (**5**) > H^B_{DA} (**6**) results in the observed back-ET trend τ_{BET} (**4**) < τ_{BET} (**5**) < τ_{BET} (**6**). As shown in Figure 12, the electronic coupling $|H^B_{DA}|$ between the
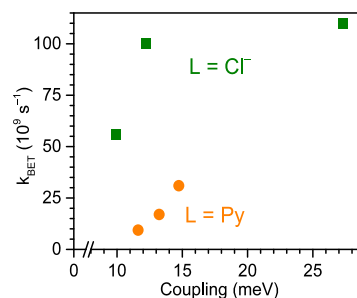
Figure 12. Comparison of electronic coupling $|H^B_{DA}|$ and back electron transfer rate k_{BET} for complexes **1**, **2**, and **3** (dark-green box solid) and **4**, **5**, and **6** (dark-orange circle solid).

$NDI^{•-}$−Ph substituent and Re(bpy)(CO)$_3$Cl at the 4-, 5-, and 6-positions of bpy is the key factor governing the rate of electron transfer.

These data illustrate that altering the substitution on the bpy core as well as changing the X ligand bound to the metal complex can increase the lifetime of Re(bpy$^{•-}$-NDI^0)(CO)$_3$X by an order of magnitude. These results will have immediate effects in the design of complexes that form donor−acceptor systems with Re(bpy)(CO)$_3$X. For example, in our previously reported complex Re(4-bpy-DPA-NDI$^{•-}$)(CO)$_3$Cl (see Figure 1), where the triad is constructed through the 4-position of bpy, moving NDI−DPA− to the 6-position of bpy, as well as changing the Cl^- ligand to pyridine would likely increase the lifetime of Re(6-bpy$^{•-}$-DPA-NDI)(CO)$_3$Py from ~25 to ~250 ns. This increase in lifetime will allow the reduced complex to compete with reactions that proceed on the diffusional time scale, such as CO_2 binding and catalysis.

■ CONCLUSIONS

In this study, we synthesized six new complexes containing an $NDI^{•-}$ chromophore bound to Re(bpy)(CO)$_3$X via a phenyl bridge. Varying the position of the NDI−Ph substituent on bpy affects the reduction potentials of Re(bpy)(CO)$_3$X. X-ray crystallography and NMR spectroscopy of model complexes show that the 6-Ph-bpy is perturbed by the metal center complex, and that the reduction of the metal complex forces the complex to Coulombically repel the phenyl substituent in the 6-Ph-bpy complex but not in the 4- and 5-Ph-bpy complexes.

Ultrafast spectroscopic experiments show that upon excitation of the $NDI^{•-}$ at 605 nm, the covalently attached Re(bpy)(CO)$_3$X is reduced to Re(bpy$^{•-}$)(CO)$_3$X in <2 ps regardless of the position of substitution. The time constant for back electron transfer τ_{BET} is larger in cationic complexes than in neutral ones. Additionally, as the location of substitution is varied from the 4 to the 5 to the 6-position on the bpy ligand, both ΔG_{BET} and τ_{BET} increase. This observation, which is contrary to expectation, is explained by decreased coupling between the NDI chromophore and the metal complex as the location of substitution goes from the 4 to the 5 to the 6-position.

This work provides key insights into creating effective donor−acceptor complexes based on the popular Re(bpy)-(CO)$_3$X CO_2 reduction catalyst. One important finding is that

incorporating a chromophore at the 4, 5, or 6-positions of bpy does not affect the quantum yield of forward electron transfer. This ensures that in photocatalytic systems, each photon that is absorbed by the $NDI^{\bullet-}$ is transferred to form $Re(bpy^{\bullet-})$-$(CO)_3X$, the first intermediate in the catalytic cycle. Second, the attachment of the $NDI^{\bullet-}-Ph$ to the 6-position of bpy does not negatively impact the reduction potential of bpy, indicating that the potency $Re(bpy^{\bullet-})(CO)_3X$ for CO_2 reduction is maintained, a failing seen in previous chromophores conjugated to the bpy. Third, incorporating the $NDI^{\bullet-}$ chromophore at the 6-position of bpy and exchanging the Cl^- ligand for pyridine leads to an order of magnitude increase in τ_{BET}. Finally, the photoinduced electron transfer recombination rates are determined either by ΔG_{BET} or by the electronic coupling between $Re(bpy^{\bullet-})(CO)_3Cl$ and NDI. This systematic approach will impact the rational design of complexes that aim to the lifetime of the reduced complex, a critical requirement for photocatalytic CO_2 reduction and artificial photosynthesis.

ASSOCIATED CONTENT

Supporting Information

The Supporting Information is available free of charge on the ACS Publications website at DOI: 10.1021/acs.jpcc.8b12264.

Synthetic procedures and spectroscopic (NMR, fsTA, nsTA, and EPR) data (PDF)

Crystallographic data (CIF)

Structure factors for datablock(s) josesample_solve (PDF)

AUTHOR INFORMATION

Corresponding Authors

*E-mail: msohail@hbku.edu.qa (M.S.).
*E-mail: m-wasielewski@northwestern.edu (M.R.W.).
*E-mail: victor.batista@yale.edu (V.S.B.).

ORCID

Jose F. Martinez: 0000-0002-1294-5920
Nathan T. La Porte: 0000-0001-7467-4460
Subhajyoti Chaudhuri: 0000-0001-8297-1123
Victor S. Batista: 0000-0002-3262-1237
Michael R. Wasielewski: 0000-0003-2920-5440

Author Contributions

∥J.F.M. and N.T.L. contributed equally to this work

Notes

The authors declare no competing financial interest.

ACKNOWLEDGMENTS

REFERENCES

(1) Barber, J.; Tran, P. D. From Natural to Artificial Photosynthesis. *J. R. Soc., Interface* **2013**, *10*, No. 20120984.

(2) Wasielewski, M. R. Energy, Charge, and Spin Transport in Molecules and Self-Assembled Nanostructures Inspired by Photosynthesis. *J. Org. Chem.* **2006**, *71*, 5051−5066.

(3) Wasielewski, M. R. Self-Assembly Strategies for Integrating Light Harvesting and Charge Separation in Artificial Photosynthetic Systems. *Acc. Chem. Res.* **2009**, *42*, 1910−1921.

(4) McConnell, I.; Li, G.; Brudvig, G. W. Energy Conversion in Natural and Artificial Photosynthesis. *Chem. Biol.* **2010**, *17*, 434−447.

(5) Hawecker, J.; Lehn, J.-M.; Ziessel, R. Efficient Photochemical Reduction of CO_2 to Co by Visible Light Irradiation of Systems Containing $Re(bipy)(CO)_3X$ or $Ru(bipy)_3^{2+}-Co^{2+}$ Combinations as Homogeneous Catalysts. *J. Chem. Soc., Chem. Commun.* **1983**, 536−538.

(6) Stor, G. J.; Hartl, F.; van Outersterp, J. W. M.; Stufkens, D. J. Spectroelectrochemical (IR, UV/Vis) Determination of the Reduction Pathways for a Series of $[Re(CO)_3(\alpha\text{-diimine})L']^{0/+}$ (L' = halide, OTf-, THF, MeCN, N-PrCN, PPh_3, $P(OMe)_3$) Complexes. *Organometallics* **1995**, *14*, 1115−1131.

(7) Tamaki, Y.; Ishitani, O. Supramolecular Photocatalysts for the Reduction of CO_2. *ACS Catal.* **2017**, *7*, 3394−3409.

(8) Clark, M. L.; Cheung, P. L.; Lessio, M.; Carter, E. A.; Kubiak, C. P. Kinetic and Mechanistic Effects of Bipyridine (bpy) Substituent, Labile Ligand, and Brønsted Acid on Electrocatalytic CO_2 Reduction by Re(bpy) Complexes. *ACS Catal.* **2018**, *8*, 2021−2029.

(9) Smieja, J. M.; Kubiak, C. P. $Re(bipy-tBu)(CO)_3Cl$—Improved Catalytic Activity for Reduction of Carbon Dioxide: IR-Spectroelectrochemical and Mechanistic Studies. *Inorg. Chem.* **2010**, *49*, 9283−9289.

(10) Hayashi, Y.; Kita, S.; Brunschwig, B. S.; Fujita, E. Involvement of a Binuclear Species with the Re−C(O)O−Re Moiety in CO_2 Reduction Catalyzed by Tricarbonyl Rhenium(I) Complexes with Diimine Ligands: Strikingly Slow Formation of the Re−Re and Re−C(O)O−Re Species from $Re(dmb)(CO)_3S$ (dmb = 4,4′-Dimethyl-2,2′-Bipyridine, S = Solvent). *J. Am. Chem. Soc.* **2003**, *125*, 11976−11987.

(11) Chabolla, S. A.; Dellamary, E. A.; Machan, C. W.; Tezcan, F. A.; Kubiak, C. P. Combined Steric and Electronic Effects of Positional Substitution on Dimethyl-Bipyridine Rhenium(I) Tricarbonyl Electrocatalysts for the Reduction of CO_2. *Inorg. Chim. Acta* **2014**, *422*, 109−113.

(12) Frayne, L.; Das, N.; Paul, A.; Amirjalayer, S.; Buma, W. J.; Woutersen, S.; Long, C.; Vos, J. G.; Pryce, M. T. Photo- and Electrochemical Properties of a CO_2 Reducing Ruthenium−Rhenium Quaterpyridine-Based Catalyst. *ChemPhotoChem* **2018**, *2*, 323−331.

(13) Gabrielsson, A.; Hartl, F.; Zhang, H.; Lindsay Smith, J. R.; Towrie, M.; Vlček, A.; Perutz, R. N. Ultrafast Charge Separation in a Photoreactive Rhenium-Appended Porphyrin Assembly Monitored by Picosecond Transient Infrared Spectroscopy. *J. Am. Chem. Soc.* **2006**, *128*, 4253−4266.

(14) Bingöl, B.; Durrell, A. C.; Keller, G. E.; Palmer, J. H.; Grubbs, R. H.; Gray, H. B. Electron Transfer Triggered by Optical Excitation of Phenothiazine-tris(meta-phenylene-ethynylene)-(tricarbonyl)-(bpy)(py)rhenium(I). *J. Phys. Chem. B* **2013**, *117*, 4177−4182.

(15) Kuramochi, Y.; Ishitani, O.; Ishida, H. Reaction Mechanisms of Catalytic Photochemical CO_2 Reduction Using Re(I) and Ru(II) Complexes. *Coord. Chem. Rev.* **2018**, *373*, 333−356.

(16) Koike, K.; Grills, D. C.; Tamaki, Y.; Fujita, E.; Okubo, K.; Yamazaki, Y.; Saigo, M.; Mukuta, T.; Onda, K.; Ishitani, O.

Investigation of Excited State, Reductive Quenching, and Intramolecular Electron Transfer of Ru(II)−Re(I) Supramolecular Photocatalysts for CO$_2$ Reduction Using Time-Resolved IR Measurements. *Chem. Sci.* **2018**, *9*, 2961−2974.

(17) La Porte, N. T.; Martinez, J. F.; Chaudhuri, S.; Hedström, S.; Batista, V. S.; Wasielewski, M. R. Photoexcited Radical Anion Super-Reductants for Solar Fuels Catalysis. *Coord. Chem. Rev.* **2018**, *361*, 98−119.

(18) Gosztola, D.; Niemczyk, M. P.; Svec, W.; Lukas, A. S.; Wasielewski, M. R. Excited Doublet States of Electrochemically Generated Aromatic Imide and Diimide Radical Anions. *J. Phys. Chem. A* **2000**, *104*, 6545−6551.

(19) Fujitsuka, M.; Kim, S. S.; Lu, C.; Tojo, S.; Majima, T. Intermolecular and Intramolecular Electron Transfer Processes from Excited Naphthalene Diimide Radical Anions. *J. Phys. Chem. B* **2015**, *119*, 7275−7282.

(20) Connelly, N. G.; Geiger, W. E. Chemical Redox Agents for Organometallic Chemistry. *Chem. Rev.* **1996**, *96*, 877−910.

(21) Young, R. M.; Dyar, S. M.; Barnes, J. C.; Juríček, M.; Stoddart, J. F.; Co, D. T.; Wasielewski, M. R. Ultrafast Conformational Dynamics of Electron Transfer in Exbox^{4+}⊂Perylene. *J. Phys. Chem. A* **2013**, *117*, 12438−12448.

(22) Horwitz, N. E.; Phelan, B. T.; Nelson, J. N.; Krzyaniak, M. D.; Wasielewski, M. R. Picosecond Control of Photogenerated Radical Pair Lifetimes Using a Stable Third Radical. *J. Phys. Chem. A* **2016**, *120*, 2841−2853.

(23) Greenfield, S. R.; Wasielewski, M. R. Optical Parametric Amplification of Femtosecond Pulses Tunable from the Blue to the Infrared with Microjoule Energies. *Appl. Opt.* **1995**, *34*, 2688−2691.

(24) Trucks, G. W.; Schlegel, H. B.; Scuseria, G. E.; Robb, M. A.; Cheeseman, J. R.; Scalmani, G.; Barone, V.; Mennucci, B.; Petersson, G. A.; Nakatsuji, H. et al. *Gaussian 09*, revision D.01; Gaussian, Inc.: Wallingford CT, 2009.

(25) Shao, Y.; Gan, Z.; Epifanovsky, E.; Gilbert, A. T.; Wormit, M.; Kussmann, J.; Lange, A. W.; Behn, A.; Deng, J.; Feng, X.; et al. Advances in Molecular Quantum Chemistry Contained in the Q-Chem 4 Program Package. *Mol. Phys.* **2015**, *113*, 184−215.

(26) Stephens, P. J.; Devlin, F. J.; Chabalowski, C. F.; Frisch, M. J. A*b Initio* Calculation of Vibrational Absorption and Circular-Dichroism Spectra Using Density-Functional Force-Fields. *J. Phys. Chem.* **1994**, *98*, 11623−11627.

(27) Tomasi, J.; Mennucci, B.; Cammi, R. Quantum Mechanical Continuum Solvation Models. *Chem. Rev.* **2005**, *105*, 2999−3094.

(28) Hay, P. J.; Wadt, W. R. Ab Initio Effective Core Potentials for Molecular Calculations. Potentials for the Transition Metal Atoms Sc to Hg. *J. Chem. Phys.* **1985**, *82*, 270−283.

(29) Marenich, A. V.; Cramer, C. J.; Truhlar, D. G. Universal Solvation Model Based on Solute Electron Density and on a Continuum Model of the Solvent Defined by the Bulk Dielectric Constant and Atomic Surface Tensions. *J. Phys. Chem. B* **2009**, *113*, 6378−6396.

(30) Cory, M. G.; Zerner, M. C. Metal-Ligand Exchange Coupling in Transition-Metal Complexes. *Chem. Rev.* **1991**, *91*, 813−822.

(31) Cossi, M.; Rega, N.; Scalmani, G.; Barone, V. Energies, Structures, and Electronic Properties of Molecules in Solution with the C-Pcm Solvation Model. *J. Comput. Chem.* **2003**, *24*, 669−681.

(32) La Porte, N. T.; Martinez, J. F.; Hedstrom, S.; Rudshteyn, B.; Phelan, B. T.; Mauck, C. M.; Young, R. M.; Batista, V. S.; Wasielewski, M. R. Photoinduced Electron Transfer from Rylenediimide Radical Anions and Dianions to Re(bpy)(CO)$_3$ Using Red and near-Infrared Light. *Chem. Sci.* **2017**, *8*, 3821−3831.

(33) Ishiyama, T.; Murata, M.; Miyaura, N. Palladium(0)-Catalyzed Cross-Coupling Reaction of Alkoxydiboron with Haloarenes: A Direct Procedure for Arylboronic Esters. *J. Org. Chem.* **1995**, *60*, 7508−7510.

(34) Takeda, H.; Koike, K.; Morimoto, T.; Inumaru, H.; Ishitani, O. *Photochemistry and Photocatalysis of Rhenium(I) Diimine Complexes*; Elsevier Inc., 2011; Vol. 63, pp 137−186.

(35) Vlček, A. Ultrafast Excited-State Processes in Re(I) Carbonyl-Diimine Complexes: From Excitation to Photochemistry. *Photophysics of Organometallics*; Springer Berlin Heidelberg: Berlin, Heidelberg, 2009; Vol. 29, pp 115−158.

(36) Constable, E. C.; Henney, R. P. G.; Leese, T. A.; Tocher, D. A. Cyclometallation Reactions of 6-Phenyl-2,2′-Bipyridine; a Potential C,N,N-Donor Analogue of 2,2′: 6′,2″-Terpyridine. Crystal and Molecular Structure of Dichlorobis(6-Phenyl-2,2′-Bipyridine)-Ruthenium(II). *J. Chem. Soc., Dalton Trans.* **1990**, 443−449.

(37) Chaudhuri, S.; Hedström, S.; Méndez-Hernández, D. D.; Hendrickson, H. P.; Jung, K. A.; Ho, J.; Batista, V. S. Electron Transfer Assisted by Vibronic Coupling from Multiple Modes. *J. Chem. Theory Comput.* **2017**, *13*, 6000−6009.

(38) Koike, K.; Naito, S.; Sato, S.; Tamaki, Y.; Ishitani, O. Architecture of Supramolecular Metal Complexes for Photocatalytic CO$_2$ Reduction: III: Effects of Length of Alkyl Chain Connecting Photosensitizer to Catalyst. *J. Photochem. Photobiol., A* **2009**, *207*, 109−114.

(39) Martinez, J. F.; La Porte, N. T.; Wasielewski, M. R. Electron Transfer from Photoexcited Naphthalene Diimide Radical Anion to Electrocatalytically Active Re(Bpy)(CO)3Cl in a Molecular Triad. *J. Phys. Chem. C* **2018**, *122*, 2608−2617.